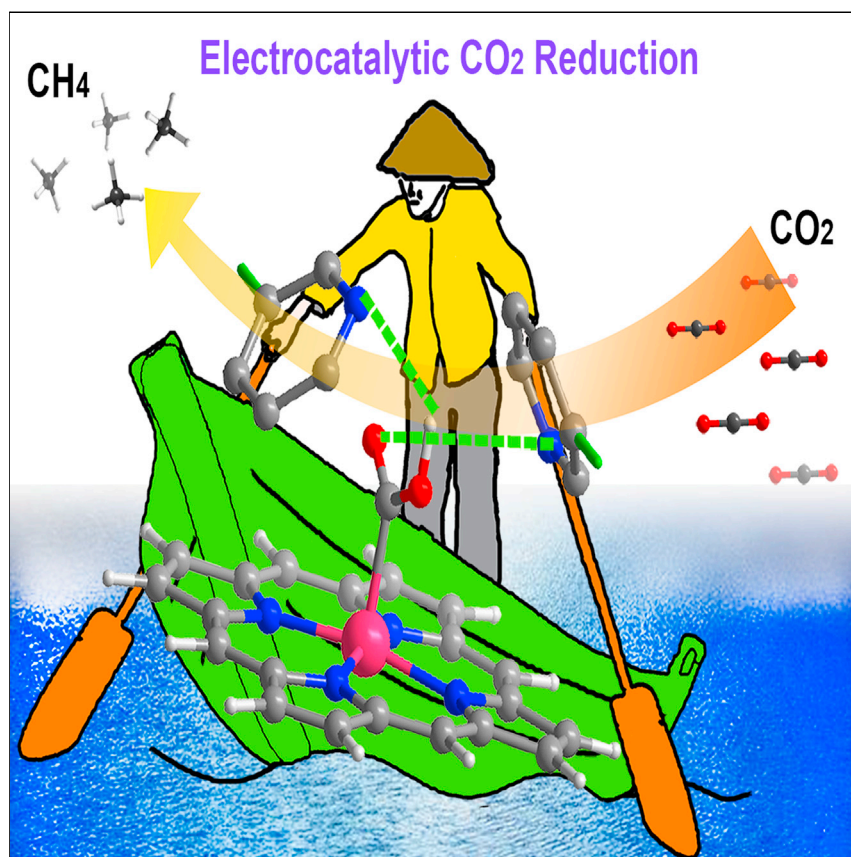


## Article

# Establishing spatially elastic hydrogen-bonding interaction in electrochemical process for selective CO<sub>2</sub>-to-CH<sub>4</sub> conversion



Sheng-Nan Sun, Jia-Ni Lu, Qi Li,  
Long-Zhang Dong, Qing Huang,  
Jiang Liu, Ya-Qian Lan

liuj@njnu.edu.cn (J.L.)  
yqqlan@m.scnu.edu.cn (Y.-Q.L.)

### Highlights

Coordination microenvironment  
around catalytic sites can affect  
product selectivity

Spatially elastic hydrogen-  
bonding interaction was  
established and studied

Well-defined catalyst model  
system catalyzes the conversion of  
CO<sub>2</sub> to CH<sub>4</sub>

Based on the crystalline Cu-based supramolecular structure, the spatially elastic hydrogen-bonding interaction between pyridine nitrogen atoms and hydrogen-donating substances (<sup>\*</sup>COOH, an important intermediate for CO<sub>2</sub> activation) was established in the electrochemical process, which can affect the adsorption energy of <sup>\*</sup>COOH and thus promote CO<sub>2</sub>-to-CH<sub>4</sub> electroreduction performance. This study provides more insights for guiding the design and synthesis of well-defined catalysts with high-performance to accurately identify the influence of subtle changes in the coordination microenvironment around catalytic active sites on the CO<sub>2</sub> electroreduction reaction.



Sun et al., Chem Catalysis 1, 1133–1144  
October 21, 2021 © 2021 Elsevier Inc.  
<https://doi.org/10.1016/j.cheecat.2021.09.003>



## Article

Establishing spatially elastic hydrogen-bonding interaction in electrochemical process for selective CO<sub>2</sub>-to-CH<sub>4</sub> conversion

Sheng-Nan Sun,<sup>1,4</sup> Jia-Ni Lu,<sup>2,4</sup> Qi Li,<sup>3,4</sup> Long-Zhang Dong,<sup>2</sup> Qing Huang,<sup>1</sup> Jiang Liu,<sup>1,2,\*</sup> and Ya-Qian Lan<sup>1,2,5,\*</sup>

## SUMMARY

In a CO<sub>2</sub> electroreduction reaction, accurately acquiring the variations of coordination microenvironment around the catalytic sites in the electrochemical process is extremely important to promote product (especially hydrocarbons) selectivity and explain the related catalytic reaction mechanism. In this work, we elaborately design and construct a simple and stable crystalline Cu-based supramolecular structure model system (including Cu-TPP, Cu-2TPyP, Cu-3TPyP, and Cu-4TPyP), in which the spatially elastic hydrogen-bonding interaction between pyridine nitrogen atom and hydrogen-donating substances (\*COOH) can be established in the electrochemical process by adjusting the position of pyridine nitrogen atoms in molecules. Based on this well-defined catalyst model system, we systematically studied the influences of variations of a spatially elastic hydrogen-bonding microenvironment on improving the CO<sub>2</sub>-to-CH<sub>4</sub> electroreduction performance. Experimental and theoretical calculation results show that subtle changes of the hydrogen-bonding interaction in the electrochemical process can affect the adsorption energy of \*COOH, thus the faradic efficiency for CH<sub>4</sub> (FE<sub>CH<sub>4</sub></sub>) can be improved from 32.3% to 62.4%.

## INTRODUCTION

Electrocatalytic CO<sub>2</sub> reduction reaction (CO<sub>2</sub>RR) driven by renewable energy is an effective method to convert CO<sub>2</sub> into various valuable products under mild conditions.<sup>1–6</sup> At present, two electron-transferred products (including carbon monoxide and formic acid) are the most common and easily produced by electrocatalytic CO<sub>2</sub>RR.<sup>7–14</sup> In comparison, electroreducing CO<sub>2</sub> to hydrocarbons with high utilization value and energy density, such as methane, is considered to be more meaningful.<sup>15–17</sup> However, it is still a great challenge to obtain hydrocarbons selectively and efficiently in CO<sub>2</sub>RR, because the formation of such products usually involves multiple protons and an electron transfer process.<sup>18–20</sup> So far, Cu-based nano- and composite materials are the most excellent electrocatalysts for realizing CO<sub>2</sub>-to-hydrocarbon conversion,<sup>21–23</sup> which have been studied to improve electrocatalytic performance from various aspects, including size effect, crystal facets and surface defects, and the microenvironment.<sup>16,24–31</sup>

In terms of the microenvironment, previous works have reported that the halogen ions added to the electrolyte can be adsorbed on the Cu surface to promote the transfer of electron charges from the Cu surface to CO<sub>2</sub>, thus increasing the yield

## The bigger picture

In the CO<sub>2</sub> electroreduction reaction, effectively monitoring the influence of variations of coordination microenvironment around catalytic sites on the related reaction mechanism is critical to improve product selectivity. However, the realization of this is still a challenge because the traditional nano- or composite catalysts often cannot provide enough clear microenvironment information. Herein, we build a crystalline Cu-based supramolecular structure model system to reveal the effect of a spatially elastic hydrogen-bonding microenvironment on converting CO<sub>2</sub> to specific hydrocarbons in an electrocatalytic process, which is achieved by adjusting the positions of pyridine nitrogen atoms in the system. This work systematically and clearly studies the important influence of the hydrogen-bonding microenvironment around catalytic sites in the electrochemical process on reaction, and it also provides more insights for guiding the design and synthesis of high-performance crystalline catalysts.



of hydrocarbons.<sup>32</sup> Moreover, adding cetyltrimethylammonium bromide (CTAB) to the electrolyte can promote the desorption of HCOO\* by competitive adsorption of CTAB, which can also improve catalytic activity.<sup>33</sup> In addition, it has been shown that adjusting the local concentration of CO<sub>2</sub> on the catalyst surface can influence the reaction kinetics of CO<sub>2</sub>, and thus significantly improve the C–C coupling.<sup>34</sup> Therefore, adjusting the microenvironment around catalytic active sites is very important for optimizing electrocatalytic CO<sub>2</sub>RR performance.<sup>27,35–37</sup> As inspired by the CO<sub>2</sub> activation process, it undergoes multiple hydrogenation steps and generates a variety of hydrogen-bonding intermediate species.<sup>38,39</sup> Therefore, if there are electronegative atoms/groups existing in the spatial coordination microenvironment around the catalytically active site, they will be very likely to form strong hydrogen bond interactions with specific hydrogen-donating intermediates (e.g., \*COOH). Under this circumstance, the spatial distance and arrangement variations of hydrogen-bonding interaction in the coordination microenvironment may greatly affect the adsorption energy of the hydrogen-bonding intermediates on the active sites of catalysts. Nevertheless, there is still lack of basic understanding of how this kind of spatially elastic hydrogen-bonding interaction affects the conversion of CO<sub>2</sub> to hydrocarbons to date. The main reason for this fact is the absence of the establishment of simple and well-defined model catalyst systems to monitor catalytic active sites and changes of the hydrogen-bonding microenvironment (involving spatial arrangement, composition, distance, etc.) accurately.

Crystalline compounds as catalysts usually have clear structural information on the active metal sites/centers and their spatial coordination microenvironment.<sup>40</sup> More importantly, they can be designed and constructed elaborately into a specific model catalyst system through strategic selection of appropriate coordination metal resources and functionalized organic ligands.<sup>41–45</sup> Therefore, they are promising for use to systematically and deeply understand the concrete influence of the hydrogen-bonding microenvironment around the catalytic sites on electrocatalytic conversion of CO<sub>2</sub> to hydrocarbons. Moreover, to establish an effective hydrogen-bonding coordination microenvironment (around the catalytic active site) with hydrogen-bonding intermediate species generated in the CO<sub>2</sub> electroreduction process, structural design characteristics for the catalysts—that there are electronegative atoms/groups that exist within a certain coordination space around the catalytic active sites—should be satisfied.<sup>46</sup> However, the crystalline catalysts for efficiently converting CO<sub>2</sub> into hydrocarbons are rarely reported so far because of their relatively low activity and structural stability.

Based on the above design, we build a stable crystalline Cu-based supramolecular structure model system (including Cu-TPP, Cu-2TPyP, Cu-3TPyP, and Cu-4TPyP). By adjusting the positions of electronegative N atoms on pyridine rings in the model system, a spatially elastic hydrogen-bonding microenvironment with different hydrogen-bonding distances and arrangement modes was established around catalytic active Cu sites to study its influence on the electrocatalytic reduction of CO<sub>2</sub> to CH<sub>4</sub>. The electrochemical characterizations and the corresponding density functional theory (DFT) calculation results demonstrate that electrocatalytic CO<sub>2</sub>RR performance is improved by two factors that importantly affect the \*COOH adsorption energy. First, spatially elastic hydrogen-bonding interactions of N–H and N–O. Based on the charge they carry, the repulsions and attractions exist, respectively, in N–O and N–H; and, since Cu-3TPyP has the shortest N–H bond and longest N–O bond (2.451 and 3.560 Å), it should bind \*COOH strongest. Second, the binding strength between Cu and C of \*COOH caused by the bond angles for N–Cu–N.

<sup>1</sup>School of Chemistry, South China Normal University, Guangzhou 510006, P.R. China

<sup>2</sup>Jiangsu Collaborative Innovation Centre of Biomedical Functional Materials, Jiangsu Key Laboratory of New Power Batteries, School of Chemistry and Materials Science, Nanjing Normal University, Nanjing 210023, P.R. China

<sup>3</sup>College of Materials Science and Engineering, Southeast University, Nanjing 211189, P.R. China

<sup>4</sup>These authors contributed equally

<sup>5</sup>Lead contact

\*Correspondence: liuj@njnu.edu.cn (J.L.), yqlan@m.scnu.edu.cn (Y.-Q.L.)

<https://doi.org/10.1016/j.cheecat.2021.09.003>

Among them, Cu-3TPyP has more bent angle ( $168.452^\circ$ ) than Cu-4TPyP ( $169.690^\circ$ ) and Cu-2TPyP ( $173.094^\circ$ ), so it can bind  $^*COOH$  strongest. Therefore, Cu-3TPyP has excellent electrocatalytic performance ( $FE_{CH_4} = 62.4\%$  at  $-1.0$  V), which is higher than Cu-4TPyP ( $FE_{CH_4} = 54.2\%$  at  $-1.0$  V), Cu-2TPyP ( $FE_{CH_4} = 32.7\%$  at  $-1.1$  V), and Cu-TPP ( $FE_{CH_4} = 32.3\%$  at  $-1.1$  V). This is the first time that a stable crystalline catalyst model system has been established to systematically and clearly reveal the influence of spatial coordination microenvironment changes of catalytic active sites in electrochemical process on  $CO_2RR$  performance.

## RESULTS AND DISCUSSION

### Structure and characterization

Cu-TPP, Cu-2TPyP, Cu-3TPyP, and Cu-4TPyP were synthesized by the different porphyrin-derived ligands (5,10,15,20-tetraphenyl-21H,23H-porphine [TPP]; 5,10,15,20-tetra(2pyridyl)-21H,23H-porphine [2TPyP]; 5,10,15,20-tetra(3pyridyl)-21H,23H-porphine [3TPyP]; 5,10,15,20-tetra(4pyridyl)-21H,23H-porphine [4TPyP]) and metal salt ( $Cu(Ac)_2 \cdot H_2O$  or  $Cu(NO_3)_2 \cdot 3H_2O$ ) under solvothermal conditions. Cu-TPP, Cu-2TPyP, and Cu-4TPyP are all black purple octahedral crystals, and Cu-3TPyP is reddish brown square crystal (Figure S1). Single-crystal X-ray diffraction analysis reveals that Cu-TPP and Cu-2TPyP crystallize in the same space group (tetragonal space group  $I-42d$ ), Cu-4TPyP crystallizes in monoclinic space group  $Cc$ , and Cu-3TPyP crystallizes in monoclinic space group  $P2_1/C$ , respectively (Table S1). The asymmetric units of crystals are shown in Figures S2 and S3. As shown in Figures 1A–1D, the whole molecular structures of four compounds are all composed of a metal Cu(II) ion and a pyridine/benzene-modified porphyrin. Among them, the Cu(II) ion is captured by the "N<sub>4</sub> pocket" of the porphyrin ring. It should be mentioned that the positions of pyridine N atoms in these four single molecules are different (Figures 1B–1D), which may be conducive to build spatially elastic hydrogen-bonding interactions. In Cu-2TPyP, the distances between the Cu ion in each porphyrin and its adjacent pyridine N atoms on the other two porphyrins are measured as  $6.2678 \text{ \AA}$  (Figure 1F). Similarly, as shown in Figures 1G and 1H, there are also two distances that can be measured for Cu-3TPyP ( $6.2974$  and  $3.9476 \text{ \AA}$ ) and Cu-4TPyP ( $5.2962$  and  $5.2513 \text{ \AA}$ ), respectively. By  $\pi$ - $\pi$  stacking and hydrogen-bonding interactions, these single molecules are further self-assembled three-dimensional structures (Figures 1I–1L). It is worth noting that there are no crystallized solvent molecules in their lattices.

The powder X-ray diffraction (PXRD) patterns of the synthesized Cu-TPP, Cu-2TPyP, Cu-3TPyP, and Cu-4TPyP are in good line with the simulated pattern obtained from single-crystal X-ray diffraction (Figures S4–S7), illustrating that they have fine crystallinity and high phase purity. The technique of pressed KBr pellets was used to perform Fourier transform infrared spectroscopy characterization of crystals. Take Cu-TPP, for example, (Figure S8), the peaks of TPP at  $3,315$  and  $966 \text{ cm}^{-1}$  are the stretching vibration peak and the bending vibration peak of N–H, respectively. In the infrared spectra of Cu-TPP, the N–H characteristic peaks at  $3,315$  and  $966 \text{ cm}^{-1}$  disappear, while a strong Cu–N stretching vibration peak appears at  $999 \text{ cm}^{-1}$ , indicating that the porphyrin ligand was indeed coordinated with the Cu ion.<sup>47</sup> Similar phenomena were observed in Cu-2TPyP, Cu-3TPyP, and Cu-4TPyP (Figures S9–S11). Thermogravimetric analysis was conducted under  $O_2$  atmosphere to study the thermal stability of these crystalline compounds (Figure S12). The results show that a stable platform can be maintained up to  $400^\circ C$ , indicating that there are no solvent molecules in the crystal lattice, which is consistent with the crystal structure data of four single molecules.

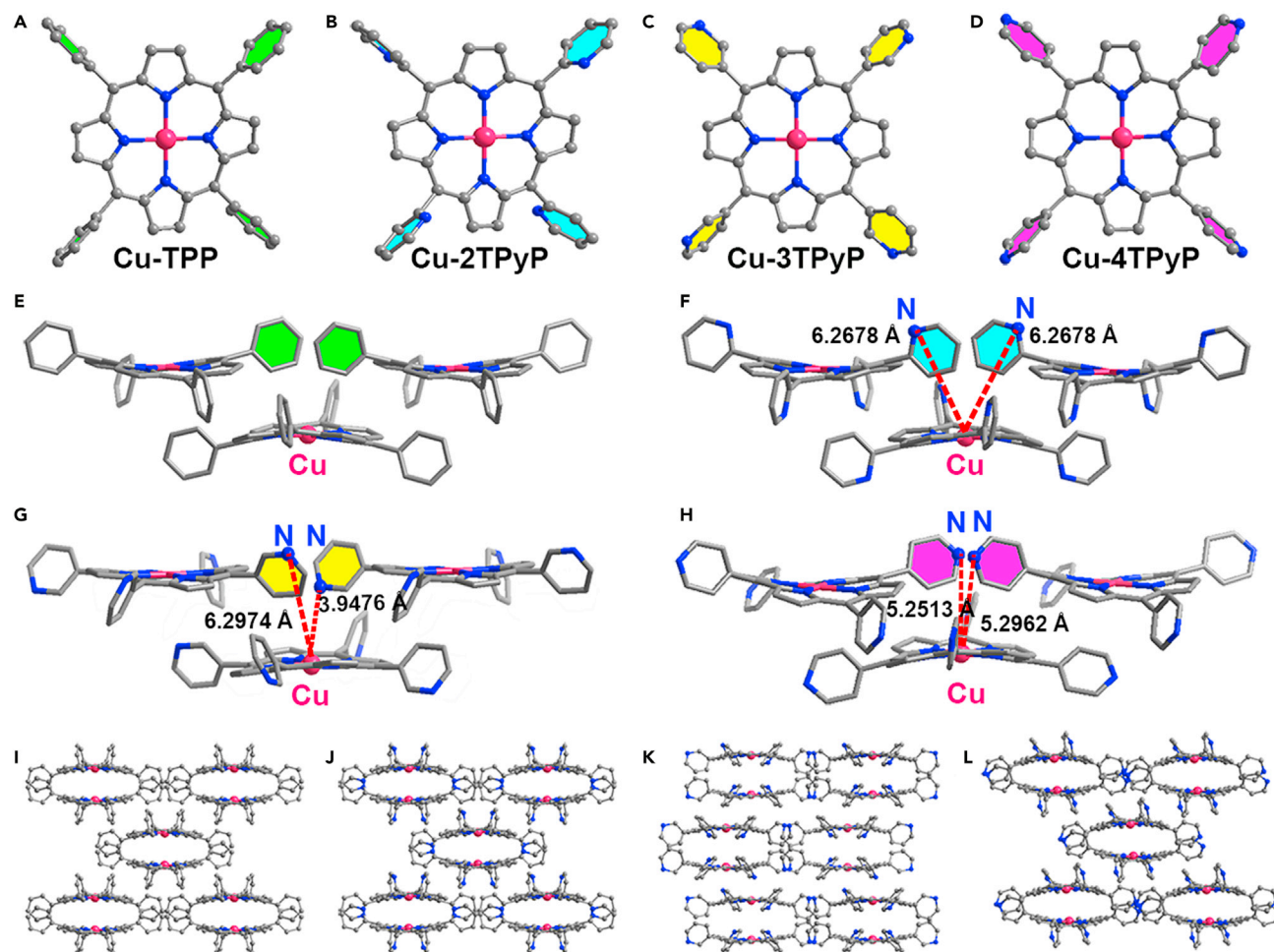


**Figure 1. The structures of crystals**

(A–D) The molecular structures of Cu-TPP (A), Cu-2TPyP (B), Cu-3TPyP (C), and Cu-4TPyP (D).

(E–H) The distances between the Cu ion in each porphyrin and its adjacent pyridine N atoms on the other two porphyrins.

(I–L) The stacked structures of Cu-TPP (I), Cu-2TPyP (J), Cu-3TPyP (K), and Cu-4TPyP (L).

C, gray; N, blue; Cu, pink.

### Electrocatalytic performance

The electrocatalytic CO<sub>2</sub>RR activities of Cu-TPP, Cu-2TPyP, Cu-3TPyP, and Cu-4TPyP were investigated by being mixed with acetylene black and deposited on a carbon-based gas diffusion electrode (GDE) with a Nafion perfluorinated resin binder in a flow cell. KOH (1 M, pH 14) was used as electrolyte. In this work, all the experiments were carried out versus a Ag/AgCl electrode and the potential results were recorded versus a reversible hydrogen electrode. Catalyst support (carbon paper) and other additives (carbon black and Nafion) have no effect on electrocatalytic CO<sub>2</sub>RR activity; as shown in Figure S13, hydrogen (H<sub>2</sub>) is the main product. Linear scanning voltammetry (LSV) under Ar and CO<sub>2</sub> atmospheres were first conducted in the range of –0.2 to –1.2 V to evaluate the electrocatalytic CO<sub>2</sub>RR performance, respectively (Figures 2A and S14–S16). It can be seen that there are significantly higher current densities under CO<sub>2</sub> atmosphere than under Ar atmosphere, indicating that Cu-TPP, Cu-2TPyP, Cu-3TPyP, and Cu-4TPyP as catalysts have a substantial catalytic effect on CO<sub>2</sub>RR rather than hydrogen evolution reaction. Besides, the current densities under the CO<sub>2</sub> atmosphere are in this

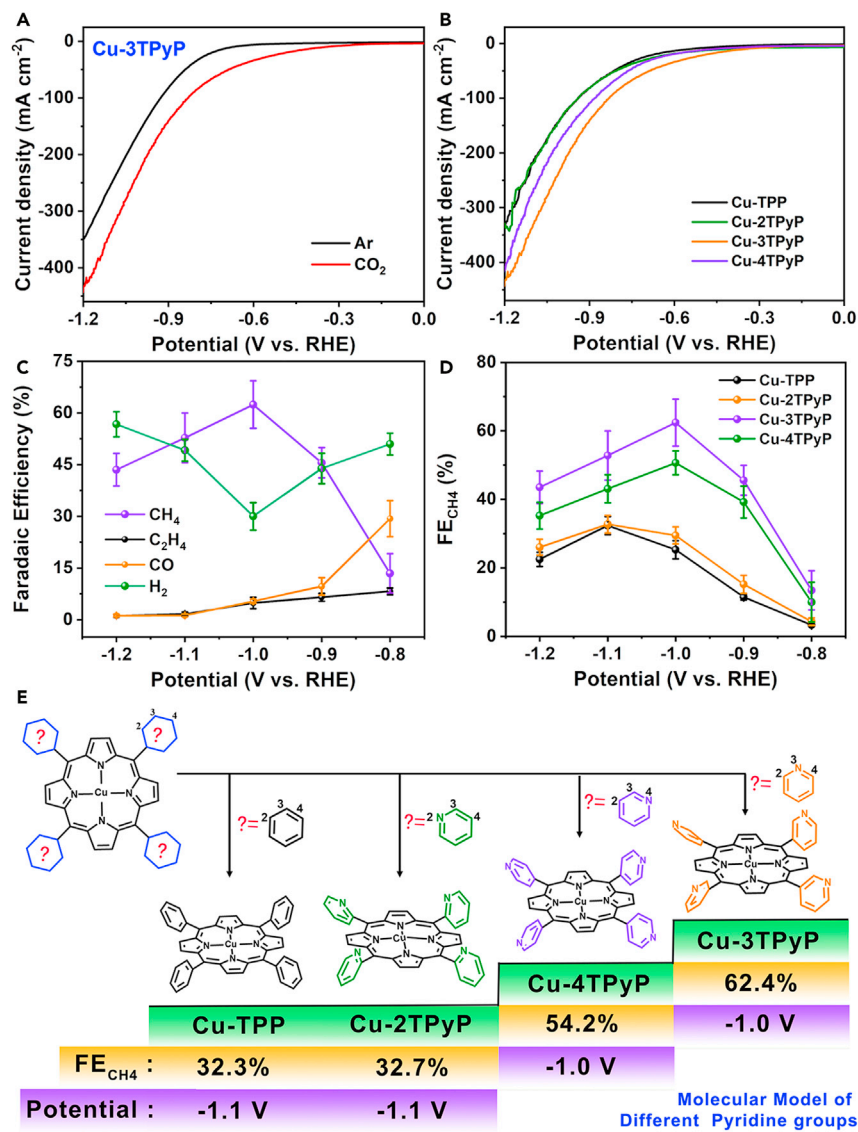


**Figure 2. Electrochemical performance**

- (A) LSVs of Cu-3TPyP in 1 M KOH solution under Ar or CO<sub>2</sub> atmosphere.  
 (B) LSVs of Cu-TPP, Cu-2TPyP, Cu-3TPyP, and Cu-4TPyP in 1 M KOH solution under CO<sub>2</sub> atmosphere.  
 (C) Faradaic efficiencies of Cu-3TPyP for CH<sub>4</sub>, C<sub>2</sub>H<sub>4</sub>, CO, and H<sub>2</sub> in 1 M KOH solution.  
 (D) FE<sub>CH<sub>4</sub></sub> of electrocatalysts at different potentials (−0.8 to −1.2 V).  
 (E) Maximum FE<sub>CH<sub>4</sub></sub> of catalysts at optimal potentials.

order: Cu-3TPyP > Cu-4TPyP > Cu-2TPyP ≈ Cu-TPP, demonstrating that Cu-3TPyP has highest electrochemical activity (Figure 2B).

Controlled potential electrolysis in the range of −0.8 to −1.2 V was conducted on the catalyst-modified GDE under CO<sub>2</sub> atmosphere to quantify the activity and selectivity of electrocatalytic CO<sub>2</sub>RR. CH<sub>4</sub>, C<sub>2</sub>H<sub>4</sub>, and CO, as gas-phase reduction products were detected by gas chromatography (Figures S17–S19). The <sup>1</sup>H nuclear magnetic resonance (<sup>1</sup>H NMR) spectrum shows that no liquid-phase reduction products were discovered (Figure S20). As shown in Figures S21 and S22, Cu-TPP was employed as

an electrocatalyst to catalytic reduction of  $\text{CO}_2$  and  $\text{CH}_4$  is the main reduction product with small amounts of  $\text{C}_2\text{H}_4$  and  $\text{CO}$ . The faradic efficiency for  $\text{CH}_4$  reaches a maximum (32.3%) at  $-1.1$  V. Cu-2TPyP exhibits similar  $\text{CO}_2\text{RR}$  properties, the maximum of  $\text{FE}_{\text{CH}_4}$  is 32.7% at  $-1.1$  V (Figures S23 and S24). In contrast to Cu-TPP and Cu-2TPyP, the  $\text{FE}_{\text{CH}_4}$  of Cu-4TPyP achieves the largest value of 54.2% at a more positive potential ( $-1.0$  V) (Figures S25 and S26), which indicates that the electrocatalytic  $\text{CO}_2\text{RR}$  performance of Cu-4TPyP is superior to that of Cu-TPP and Cu-2TPyP. As for Cu-3TPyP, the electrocatalytic  $\text{CO}_2\text{RR}$  performance is further improved (Figures 2C and S27). As seen from Figure 2D, the selectivity of  $\text{CH}_4$  in the reduction products is higher than the other three comparison samples (Cu-TPP, Cu-2TPyP, and Cu-4TPyP). At  $-1.0$  V, the  $\text{FE}_{\text{CH}_4}$  of Cu-3TPyP can reach more than 60% (Figure 2E). Notably, the  $\text{FE}_{\text{CH}_4}$  of Cu-3TPyP at applied potential ( $-0.9$  to  $-1.2$  V) is higher than 40%, which is even higher than the best  $\text{FE}_{\text{CH}_4}$  of Cu-TPP (32.3%) and Cu-2TPyP (32.7%) (Figure 2D).

To shed further light on the  $\text{CO}_2\text{RR}$  performance of Cu-TPP, Cu-2TPyP, Cu-3TPyP, and Cu-4TPyP, partial current density corresponding to  $\text{CH}_4$  product ( $j_{\text{CH}_4}$ ) is derived (Figure 3A). It is noteworthy that the absolute value of  $j_{\text{CH}_4}$  increases with the order of Cu-TPP/Cu-2TPyP < Cu-4TPyP < Cu-3TPyP. Take the  $j_{\text{CH}_4}$  at  $-1.0$  V as an example, Cu-3TPyP can reach  $-143.1$   $\text{mA cm}^{-2}$ , which is about 1.6 times higher than Cu-4TPyP ( $-88.6$   $\text{mA cm}^{-2}$ ), 3.6 times higher than Cu-2TPyP ( $-40.1$   $\text{mA cm}^{-2}$ ), and 4 times higher than Cu-TPP ( $-34.9$   $\text{mA cm}^{-2}$ ). Besides, the turnover frequency of Cu-3TPyP ( $908.14$   $\text{h}^{-1}$  at  $-1.0$  V) shown in Figure S28 is also higher than Cu-TPP ( $219.91$   $\text{h}^{-1}$ ), Cu-2TPyP ( $254.71$   $\text{h}^{-1}$ ), and Cu-4TPyP ( $561.92$   $\text{h}^{-1}$ ). The cyclic voltammograms were measured in the non-faradic range of  $-0.1$  to  $0.0$  V versus Ag/AgCl to obtain the electrochemical double-layer capacitance ( $C_{\text{dl}}$ ). The electrochemical surface areas (ECSA) are calculated based on  $C_{\text{dl}}$ , which is proportional to the ECSA of catalysts (Figures 3B and S29).<sup>48</sup> The  $C_{\text{dl}}$  for Cu-3TPyP is assessed to be  $15.39$   $\text{mF cm}^{-2}$ , which is larger than Cu-4TPyP ( $12.62$   $\text{mF cm}^{-2}$ ) and nearly twice as large as that of Cu-TPP ( $7.88$   $\text{mF cm}^{-2}$ ) and Cu-2TPyP ( $8.08$   $\text{mF cm}^{-2}$ ), proving that a richer accessible surface could be provided in reduction reactions. This may be one of the reasons for superior catalytic performance. To probe into the kinetics of electrolytic  $\text{CO}_2\text{RR}$ , electrochemical impedance spectroscopy measurements were conducted to evaluate the charge transfer resistance (Figure 3C). The charge transfer resistance of Cu-3TPyP ( $R_{\text{ct}} = 6.87$   $\Omega$ ) is smaller than that of Cu-TPP ( $R_{\text{ct}} = 30.82$   $\Omega$ ), Cu-2TPyP ( $R_{\text{ct}} = 23.91$   $\Omega$ ), and Cu-4TPyP ( $R_{\text{ct}} = 16.60$   $\Omega$ ), indicating that the shuttle of charge transfer on Cu-3TPyP is faster (see fitting curve in Figure S30). As a result, Cu-3TPyP possesses smaller ohmic loss, exhibiting higher selectivity and activity than Cu-TPP, Cu-2TPyP, and Cu-4TPyP in  $\text{CO}_2\text{RR}$ .

To verify the carbon source of reduction products during the  $\text{CO}_2\text{RR}$  process, an isotopic experiment was performed using  $^{13}\text{CO}_2$  as a substitute for  $^{12}\text{CO}_2$ . The products were analyzed by gas chromatography-mass spectrometry. As shown in Figures 3D, S31, and S32, the peaks at  $m/z = 17$ ,  $30$ , and  $29$  are assigned to  $^{13}\text{CH}_4$ ,  $^{13}\text{C}_2\text{H}_4$ , and  $^{13}\text{CO}$ , respectively, which fully proves that the carbon sources of  $\text{CH}_4$ ,  $\text{C}_2\text{H}_4$ , and  $\text{CO}$  indeed derive from the  $\text{CO}_2$  used in the experiments.

To determine the catalytic active site of catalysts, pure porphyrin monomers without metal ions (TPP, 2TPyP, 3TPyP, and 4TPyP) were used as catalysts for the electrocatalytic  $\text{CO}_2\text{RR}$  test. The test results show that  $\text{H}_2$  is the dominant product at each applied potential ( $-0.8$  to  $-1.2$  V) (Figure S33), indicating that Cu active sites in the center of porphyrins is responsible for the observed electrocatalytic activity. Catalytic stability is an important indicator for studying electrolytic  $\text{CO}_2\text{RR}$ . As indicated

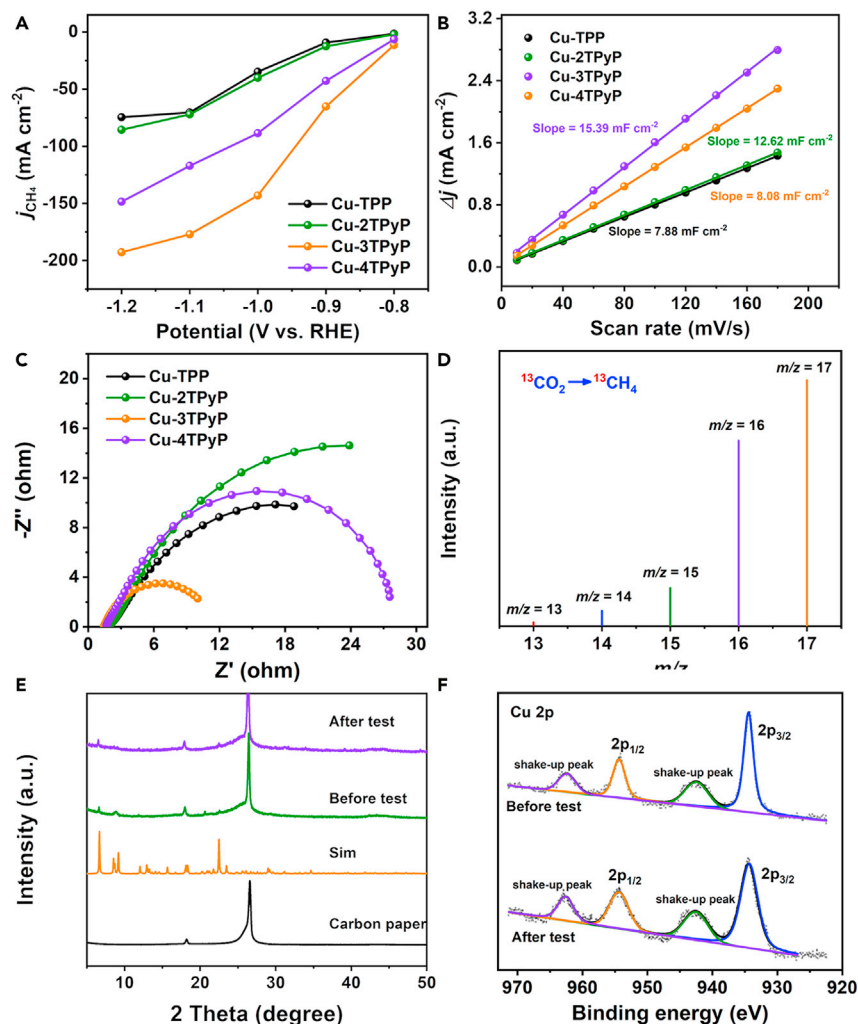


**Figure 3. Electrochemical performance and characterizations after the test**

- (A)  $j_{\text{CH}_4}$  of Cu-TPP, Cu-2TPyP, Cu-3TPyP, and Cu-4TPyP.  
 (B)  $C_{\text{dl}}$  of Cu-TPP, Cu-2TPyP, Cu-3TPyP, and Cu-4TPyP.  
 (C) Nyquist plots of electrocatalysts over the frequency ranging from 1,000 kHz to 0.1 Hz.  
 (D) The mass spectra of  $^{13}\text{CH}_4$  recorded under  $^{13}\text{CO}_2$  atmosphere.  
 (E) The PXRD patterns of electrocatalyst Cu-3TPyP after the test.  
 (F) The XPS spectra of Cu-3TPyP before and after the test.

in Figure S34, no significant attenuation of the current density ( $>200 \text{ mA cm}^{-2}$ ) is found at more than 3,600 s and  $\text{FE}_{\text{CH}_4}$  of Cu-3TPyP is stable with a small decay of 7% during 3,600 s. The SEM images of electrocatalysts before and after electrolysis are shown in Figures S35–S38. To further reveal the stability of electrocatalysts in the electrocatalytic  $\text{CO}_2\text{RR}$  process, the PXRD and XPS patterns after electrolysis experiment were compared with the simulated patterns and before the test. The results show that the corresponding diffraction peaks of crystal catalysts in PXRD did not change significantly after electrocatalytic reaction, illustrating that the structures of Cu-TPP, Cu-2TPyP, Cu-3TPyP, and Cu-4TPyP are stable during the  $\text{CO}_2\text{RR}$  process (Figures 3E and S39–S41). Also, Figure 3D shows the Cu 2p XPS spectra of Cu-3TPyP before and after the test. The BE peak at 933.6 eV of Cu  $2p_{3/2}$  corresponds to the oxidant state of Cu(II) in Cu-3TPyP, which is unchanged after electrolysis, indicating that the structure of the electrocatalyst is stable.<sup>49</sup> Because Cu(I) and Cu(0) are

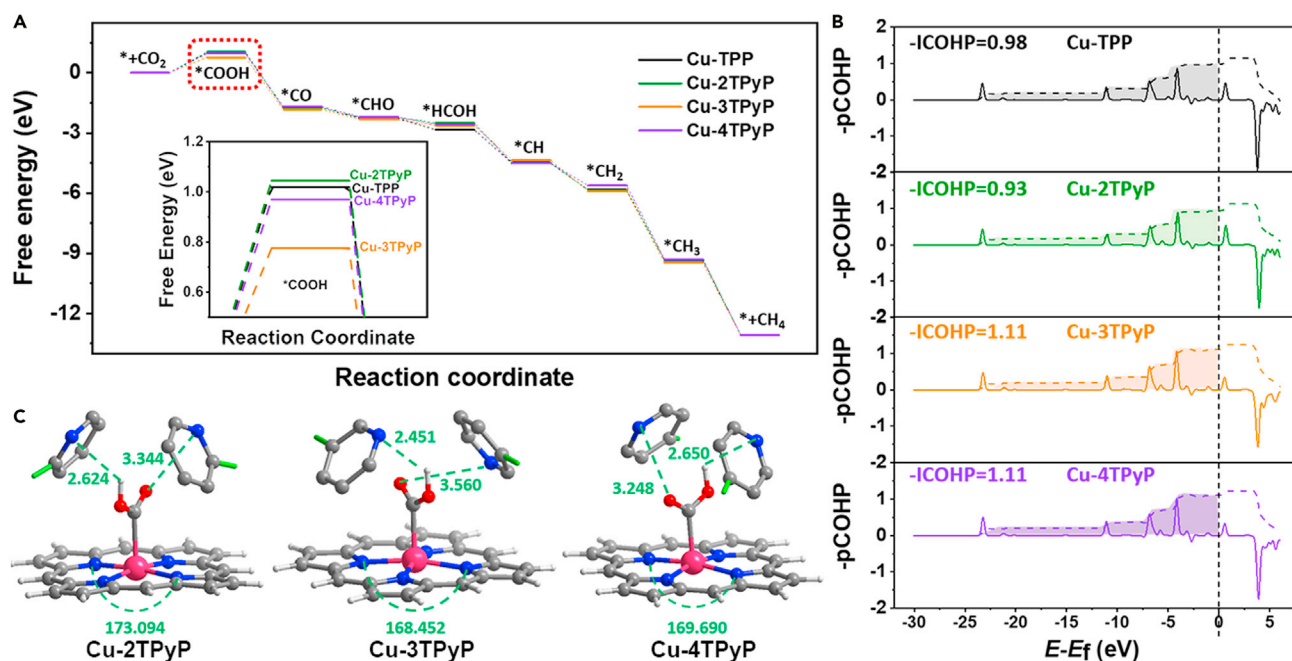


**Figure 4. DFT calculations**

(A) Free energy diagram (FED) of CO<sub>2</sub>RR to CH<sub>4</sub> in Cu-TPP (black), Cu-2TPyP (green), Cu-3TPyP (orange), and Cu-4TPyP (purple). The potential is set at  $-1.0$  V during composing FED.

(B) The optimized structure of \*COOH adsorbed on Cu-2TPyP, Cu-3TPyP, and Cu-4TPyP.

(C) The COHP of Cu-TPP, Cu-2TPyP, Cu-3TPyP, and Cu-4TPyP for the Cu-C(OOH) bond.

difficult to distinguish by Cu 2p<sub>3/2</sub> XPS, the Cu LMM Auger spectra (Figure S42) was further operated to reveal the valence states of Cu species after electroreduction treatment. The result shows that a Cu(I) peak at 569.5 eV and a Cu(0) peak at 567.7 eV were negligible, suggesting that no Cu(I) and Cu(0) species were generated.<sup>50,51</sup> Moreover, HR-TEM investigation revealed no formation of Cu nanoparticles (Figure S43). The performance of other reported crystalline compound electrocatalysts in the electroreduction of CO<sub>2</sub> to CH<sub>4</sub> is listed in Table S2.

### DFT calculations

To make a thorough inquiry into the causes of performance differences and better understand the catalysis process, DFT calculations were performed. Calculation summary: we used porphyrin Cu and its surrounding pyridine/benzene rings from another molecule as a model, while ignoring other parts far from the reaction center. In addition, it is important to note that the pyridine/benzene rings are connected to another porphyrin molecule through a C-C bond, so during adsorption, due to the repulsion effect, it will rotate around the C-C bond as the axis (Figure S44). In order to simulate this rotation, we replaced the C-C bond with a C-H bond, and fixed the C-H bond during the optimization process. A computational hydrogen electrode method was introduced to calculate the free energy diagram of CO<sub>2</sub>RR toward methane (the associated calculation details are listed in the supplemental information). As shown in Figure 4A, for all the structures, all the elementary steps are exothermic except for the first one, suggesting that the first step is the rate-determining step in the pathway to CH<sub>4</sub>. This order of free energy (Cu-TPP  $\approx$  Cu-2TPyP < Cu-4TPyP < Cu-3TPyP) can be seen in Figure 4A, which is consistent with the experiments. This indicates that the experimental order could be attributed to the same order for \*COOH adsorption.

Generally, pyridine N can help the adsorption of \*COOH, which has been proved in some former work.<sup>52,53</sup> This is the reason why Cu-TPP performs relatively poorly among the four. More specifically, why \*COOH adsorption energy has such an order could be explained by two factors: (1) the spatial elastic hydrogen-bonding effect between N–H and N–O, and (2) the binding strength between Cu and C of \*COOH. For the former, we first focus on the interaction generated between N–H and N–O bonds, where H is in \*COOH, the N is in pyridine, and the O is in carbonyl of \*COOH. Considering that their distances are too far to form chemical bonds, and that they both carry large amounts of charges (+0.49, –0.48, and –0.47, for H, N, and O by Bader analysis, respectively), the interactions between N and H, and N and O, are hydrogen-bonding-like interactions. Based on the charge they carry, the repulsions and attractions exist, respectively, in N–O and N–H. Then, since Cu-3TPyP has the shortest N–H bond and longest N–O bond (2.451 and 3.56 Å), i.e., the strongest attraction and the weakest repulsion, it should bind \*COOH strongest; as for Cu-2TPyP and Cu-4TPyP, their N–H distances are close (2.624 versus 2.650 Å), but the N–O distance is slightly larger in Cu-4TPyP (3.248 versus 3.344 Å), which makes \*COOH adsorption more favorable on Cu-4TPyP. Besides the hydrogen bonding, there is another effect, namely, the Cu–C bond strength. Different from N–H and N–O, Cu–C forms a chemical bond. Therefore, the coordination environment of Cu can notably affect the adsorption energy. From Figure 4B, it is found the bond angles for N–Cu–N are slightly decreased in Cu-3TPyP and Cu-4TPyP compared with Cu-2TPyP (168.452° and 169.690° versus 173.094°). This suggests that, in Cu-3TPyP and Cu-4TPyP, the coordination environment of Cu has changed slightly from octahedral to tetrahedral, which, according to crystal field theory, suggests a lessened energy of the  $d_z^2$  orbital of Cu that is closely related with Cu–C bond, which will benefit the \*COOH adsorption. Consistently, in Figure 4C, we show that Cu–C in Cu-4TPyP and Cu-3TPyP possess higher values of integrated crystal orbital Hamilton population than in Cu-TPP and Cu-2TPyP, which again confirms the stronger binding of Cu–C in Cu-4TPyP and Cu-3TPyP. Of course, the reason that causes such binding could be attributed to the more “bent” N–Cu–N bond in Cu-4TPyP and Cu-3TPyP. More intrinsically, we guess it is the higher van der Waals repulsion between the pyridine and porphyrin, which bends the N–Cu–N bond angles. So, to recap, it is (1) the better hydrogen binding effect between N–H and N–O and (2) the more bent N–Cu–N angle in Cu-4TPyP and Cu-3TPyP that results in a better electrocatalytic CO<sub>2</sub>RR performance.

To see the possible C–C bond rotations at room temperature, as well as their impact on the adsorption energy, we have additionally implemented ab initio molecular dynamics simulation. We found that, for pyridine branches on Cu-3TPyP (denoted as 3-Py), the rotation angle is no larger than 50°; and, in most cases (>70%), the rotation is within 20° (see Figures S45 and S46 for details). This indicates that the rotation is strongly constrained at room temperature, and its impact should be negligible.

## Conclusions

Taken together, a series of stable and well-defined Cu metalloporphyrins (Cu-TPP, Cu-2TPyP, Cu-3TPyP, and Cu-4TPyP) were established as a crystalline supramolecular structure model system to study the effects of spatial elastic hydrogen-bonding interactions around the catalytic active site on the performance of electroreducing CO<sub>2</sub> to CH<sub>4</sub>. In this system, Cu-3TPyP shows the highest FE<sub>CH<sub>4</sub></sub> (62.4% at –1.0 V), followed by Cu-4TPyP (54.2% at –1.0 V) and Cu-2TPyP (32.7% at –1.1 V)/Cu-TPP (32.3% at –1.1 V). The corresponding DFT calculation results indicate that CO<sub>2</sub>RR performance is improved by two factors associated with improving \*COOH adsorption energy: (1) hydrogen-bonding effects of N–H and N–O, (2) strong binding

strength between Cu and C of \*COOH caused by the more bent N–Cu–N angle. This work can serve as an important case study for using a simple crystalline supramolecular model system to accurately identify the influence of subtle changes in microenvironment on the electrocatalytic CO<sub>2</sub>RR process.

## EXPERIMENTAL PROCEDURES

### Resource availability

#### Lead contact

Further information and requests for resources should be directed to and will be fulfilled by the lead contact, Ya-Qian Lan ([yqlan@njnu.edu.cn](mailto:yqlan@njnu.edu.cn); [yqlan@m.scnu.edu.cn](mailto:yqlan@m.scnu.edu.cn)).

#### Materials availability

All materials generated in this study are available from the lead contact without restriction.

#### Data and code availability

The accession numbers for the crystal structure CIF reported in this paper are CCDC 2056589, 2056590, and 2056591 for Cu-2TPyP, Cu-3TPyP, and Cu-4TPyP, respectively.

### Materials

Porphyrin ligands were obtained from commercial sources. Copper acetate monohydrate (Cu(Ac)<sub>2</sub>·H<sub>2</sub>O), copper nitrate trihydrate (Cu(NO<sub>3</sub>)<sub>2</sub>·3H<sub>2</sub>O), potassium hydroxide (KOH), triethylamine, *N,N*-dimethylformamide (DMF), dimethyl sulfoxide (DMSO), pyrrole, and hydrochloric acid (HCl) were supplied by the Shanghai Reagent Factory. 2-Pyridinecarboxaldehyde and Nafion solution (5 wt %) were purchased from Sigma-Aldrich. Carbon paper was bought from a fuel cell store. All chemicals used in this experiment were of analytical grade and used without further purification. All aqueous solutions were prepared with Millipore water (18.25 MΩ·cm).

### Synthesis of Cu-TPP

TPP (0.06 g, 0.10 mmol) was added into a 10 mL scintillation vial containing DMF (6 mL) and triethylamine (28 μL) with stirring for 30 min. Then, Cu(Ac)<sub>2</sub>·H<sub>2</sub>O (0.04 g, 0.20 mmol) was added into the above mixture and stirred for another 30 min. The vial was put in an oven and heated at 150°C for 72 h. Black octahedral crystals were obtained after cooling to room temperature.

### Synthesis of Cu-2TPyP

Cu(Ac)<sub>2</sub>·H<sub>2</sub>O (0.008 g, 0.04 mmol) was dissolved in DMF (2 mL) and placed into a 10 mL scintillation vial. Then 2-pyridinecarboxaldehyde (28 μL), HCl (50 μL), and DMSO (160 μL) were added successively under continuous stirring. Subsequently, pyrrole (28 μL) was added into the above solution in an argon atmosphere and heated at 120°C for 3 days. Black octahedral crystals were obtained.

### Synthesis of Cu-3TPyP

3TPyP (0.06 g, 0.10 mmol) and Cu(NO<sub>3</sub>)<sub>2</sub>·3H<sub>2</sub>O (0.097 g, 0.40 mmol) were added into DMF (6 mL) containing HCl (1 mL). The mixture was placed in a 10 mL scintillation vial and heated at 120°C for 3 days. Finally, reddish brown square crystals were obtained, washed by DMF, and air dried.

### Synthesis of Cu-4TPyP

DMF (2 mL) containing 4TPyP (6 mg, 0.01 mmol) and Cu(Ac)<sub>2</sub>·H<sub>2</sub>O (8 mg, 0.04 mmol) was placed into a 10 mL scintillation vial, then HCl (50 μL) was added with stirring for

30 min and heated at 100°C for 4 days. After cooling to room temperature at a rate of 10°C h<sup>-1</sup>, the black octahedral crystals were collected and washed with DMF several times.

### SUPPLEMENTAL INFORMATION

Supplemental information can be found online at <https://doi.org/10.1016/j.checat.2021.09.003>.

### ACKNOWLEDGMENTS

This work was financially supported by the NSFC (no. 21871141, 92061101). The project was funded by the China Postdoctoral Science Foundation (nos. 2018M630572 and 2020M682749), Guangdong Basic and Applied Basic Research Foundation (no. 2020A1515110836), Priority Academic Program Development of Jiangsu Higher Education Institutions, and the Foundation of Jiangsu Collaborative Innovation Center of Biomedical Functional Materials.

### AUTHOR CONTRIBUTIONS

Y.-Q.L. and J.L. conceived and designed the idea. S.-N.S., J.-N.L., and Q.L. designed the experiments, conducted the characterizations, and analyzed the data. L.-Z.D. and Q.H. analyzed the crystallographic data. S.-N.S. wrote the manuscript. All the authors reviewed and contributed to this paper.

### DECLARATION OF INTERESTS

The authors declare no competing interests.

Received: June 7, 2021

Revised: August 7, 2021

Accepted: September 3, 2021

Published: October 11, 2021

### REFERENCES

- Li, J., Chen, G., Zhu, Y., Liang, Z., Pei, A., Wu, C.-L., Wang, H., Lee, H.R., Liu, K., Chu, S., and Cui, Y. (2018). Efficient electrocatalytic CO<sub>2</sub> reduction on a three-phase interface. *Nat. Catal.* *1*, 592–600.
- Dinh, C.-T., Burdyny, T., Kibria, M.G., Seifitokaldani, A., Gabardo, C.M., Garcia de Arquer, F.P., Kiani, A., Edwards, J.P., De Luna, P., Bushuyev, O.S., et al. (2018). CO<sub>2</sub> electroreduction to ethylene via hydroxide-mediated copper catalysis at an abrupt interface. *Science* *360*, 783.
- Vasileff, A., Zhu, Y., Zhi, X., Zhao, Y., Ge, L., Chen, H.M., Zheng, Y., and Qiao, S.-Z. (2020). Electrochemical reduction of CO<sub>2</sub> to ethane through stabilization of an ethoxy intermediate. *Angew. Chem. Int. Ed. Engl.* *59*, 19649–19653.
- Xu, C., Vasileff, A., Zheng, Y., and Qiao, S.-Z. (2020). Recent progress of 3d transition metal single-atom catalysts for electrochemical CO<sub>2</sub> reduction. *Adv. Mater. Inter.* *8*, 2001904.
- Ji, L., Li, L., Ji, X., Zhang, Y., Mou, S., Wu, T., Liu, Q., Li, B., Zhu, X., Luo, Y., et al. (2020). Highly selective electrochemical reduction of CO<sub>2</sub> to alcohols on an FeP nanoarray. *Angew. Chem. Int. Ed. Engl.* *59*, 758–762.
- Zhao, R., Ding, P., Wei, P., Zhang, L., Liu, Q., Luo, Y., Li, T., Lu, S., Shi, X., Gao, S., et al. (2021). Recent progress in electrocatalytic methanation of CO<sub>2</sub> at ambient conditions. *Adv. Funct. Mater.* *31*, 2009449.
- Han, N., Ding, P., He, L., Li, Y., and Li, Y. (2020). Promises of main group metal-based nanostructured materials for electrochemical CO<sub>2</sub> reduction to formate. *Adv. Energy Mater.* *10*, 1902338.
- Zhou, Y., Zhou, R., Zhu, X., Han, N., Song, B., Liu, T., Hu, G., Li, Y., Lu, J., and Li, Y. (2020). Mesoporous PdAg nanospheres for stable electrochemical CO<sub>2</sub> reduction to formate. *Adv. Mater.* *32*, 2000992.
- Ly, F., Han, N., Qiu, Y., Liu, X., Luo, J., and Li, Y. (2020). Transition metal macrocycles for heterogeneous electrochemical CO<sub>2</sub> reduction. *Coordin. Chem. Rev.* *422*, 213435.
- Han, N., Sun, M., Zhou, Y., Xu, J., Cheng, C., Zhou, R., Zhang, L., Luo, J., Huang, B., and Li, Y. (2020). Alloyed palladium-silver nanowires enabling ultrastable carbon dioxide reduction to formate. *Adv. Mater.* *33*, 2005821.
- Zheng, T., Jiang, K., Ta, N., Hu, Y., Zeng, J., Liu, J., and Wang, H. (2019). Large-scale and highly selective CO<sub>2</sub> electrocatalytic reduction on nickel single-atom catalyst. *Joule* *3*, 265–278.
- Wang, Y.-R., Huang, Q., He, C.-T., Chen, Y., Liu, J., Shen, F.-C., and Lan, Y.-Q. (2018). Oriented electron transmission in polyoxometalate-metalloporphyrin organic framework for highly selective electroreduction of CO<sub>2</sub>. *Nat. Commun.* *9*, 4466.
- Mou, S., Li, Y., Yue, L., Liang, J., Luo, Y., Liu, Q., Li, T., Lu, S., Asiri, A.M., Xiong, X., et al. (2021). Cu<sub>2</sub>Sb decorated Cu nanowire arrays for selective electrocatalytic CO<sub>2</sub> to CO conversion. *Nano Res.* *14*, 2831–2836.
- Ding, P., Zhao, H., Li, T., Luo, Y., Fan, G., Chen, G., Gao, S., Shi, X., Lu, S., and Sun, X. (2020). Metal-based electrocatalytic conversion of CO<sub>2</sub> to formic acid/formate. *J. Mater. Chem. A* *8*, 21947–21960.
- Gao, D., Arán-Ais, R.M., Jeon, H.S., and Roldan Cuenya, B. (2019). Rational catalyst and electrolyte design for CO<sub>2</sub> electroreduction towards multicarbon products. *Nat. Catal.* *2*, 198–210.
- Wang, Y., Chen, Z., Han, P., Du, Y., Gu, Z., Xu, X., and Zheng, G. (2018). Single-atomic Cu with multiple oxygen vacancies on ceria for

- electrocatalytic CO<sub>2</sub> reduction to CH<sub>4</sub>. *ACS Catal.* **8**, 7113–7119.
17. Yang, H., Wu, Y., Li, G., Lin, Q., Hu, Q., Zhang, Q., Liu, J., and He, C. (2019). Scalable production of efficient single-atom copper decorated carbon membranes for CO<sub>2</sub> electroreduction to methanol. *J. Am. Chem. Soc.* **141**, 12717–12723.
18. Vasileff, A., Xu, C., Jiao, Y., Zheng, Y., and Qiao, S.-Z. (2018). Surface and interface engineering in copper-based bimetallic materials for selective CO<sub>2</sub> electroreduction. *Chem* **4**, 1809–1831.
19. Li, F., Thevenon, A., Rosas-Hernández, A., Wang, Z., Li, Y., Gabardo, C.M., Ozden, A., Dinh, C.T., Li, J., Wang, Y., et al. (2020). Molecular tuning of CO<sub>2</sub>-to-ethylene conversion. *Nature* **577**, 509–513.
20. Ma, W., Xie, S., Liu, T., Fan, Q., Ye, J., Sun, F., Jiang, Z., Zhang, Q., Cheng, J., and Wang, Y. (2020). Electrocatalytic reduction of CO<sub>2</sub> to ethylene and ethanol through hydrogen-assisted C–C coupling over fluorine-modified copper. *Nat. Catal.* **3**, 478–487.
21. Li, Y., Xu, A., Lum, Y., Wang, X., Hung, S.-F., Chen, B., Wang, Z., Xu, Y., Li, F., Abed, J., et al. (2020). Promoting CO<sub>2</sub> methanation via ligand-stabilized metal oxide clusters as hydrogen-donating motifs. *Nat. Commun.* **11**, 6190.
22. Luo, M., Wang, Z., Li, Y.C., Li, J., Li, F., Lum, Y., Nam, D.-H., Chen, B., Wicks, J., Xu, A., et al. (2019). Hydroxide promotes carbon dioxide electroreduction to ethanol on copper via tuning of adsorbed hydrogen. *Nat. Commun.* **10**, 5814.
23. Vasileff, A., Zhi, X., Xu, C., Ge, L., Jiao, Y., Zheng, Y., and Qiao, S.-Z. (2019). Selectivity control for electrochemical CO<sub>2</sub> reduction by charge redistribution on the surface of copper alloys. *ACS Catal.* **9**, 9411–9417.
24. Nitopi, S., Bertheussen, E., Scott, S.B., Liu, X., Engstfeld, A.K., Horch, S., Seger, B., Stephens, I.E.L., Chan, K., Hahn, C., et al. (2019). Progress and perspectives of electrochemical CO<sub>2</sub> reduction on copper in aqueous electrolyte. *Chem. Rev.* **119**, 7610–7672.
25. Hahn, C., Hatsukade, T., Kim, Y.-G., Vailionis, A., Baricuauro, J.H., Higgins, D.C., Nitopi, S.A., Soriaga, M.P., and Jaramillo, T.F. (2017). Engineering Cu surfaces for the electrocatalytic conversion of CO<sub>2</sub>: controlling selectivity toward oxygenates and hydrocarbons. *PNAS* **114**, 5918.
26. Huang, Y., Handoko, A.D., Hirunsit, P., and Yeo, B.S. (2017). Electrochemical reduction of CO<sub>2</sub> using copper single-crystal surfaces: effects of CO\* coverage on the selective formation of ethylene. *ACS Catal.* **7**, 1749–1756.
27. Xing, Z., Hu, L., Ripatti, D.S., Hu, X., and Feng, X. (2021). Enhancing carbon dioxide gas-diffusion electrolysis by creating a hydrophobic catalyst microenvironment. *Nat. Commun.* **12**, 136.
28. Reske, R., Mistry, H., Beharfarid, F., Roldan Cuenya, B., and Strasser, P. (2014). Particle size effects in the catalytic electroreduction of CO<sub>2</sub> on Cu nanoparticles. *J. Am. Chem. Soc.* **136**, 6978–6986.
29. Huang, Q., Niu, Q., Ma, N.-N., Dong, L.-Z., Li, S.-L., Li, D.-S., Cai, Y.-P., and Lan, Y.-Q. (2020). Axial Cl/Br atom-mediated CO<sub>2</sub> electroreduction performance in a stable porphyrin-based metal–organic framework. *Chem. Commun.* **56**, 14817–14820.
30. Chang, X., Wang, T., Zhao, Z.-J., Yang, P., Greeley, J., Mu, R., Zhang, G., Gong, Z., Luo, Z., Chen, J., et al. (2018). Tuning Cu/Cu<sub>2</sub>O interfaces for the reduction of carbon dioxide to methanol in aqueous solutions. *Angew. Chem. Int. Ed. Engl.* **57**, 15415–15419.
31. Zhu, C., Zhang, Z., Zhong, L., Hsu, C.-S., Xu, X., Li, Y., Zhao, S., Chen, S., Yu, J., Chen, S., et al. (2020). Product-specific active site motifs of Cu for electrochemical CO<sub>2</sub> reduction. *Chem* **7**, 406–420.
32. Varela, A.S., Ju, W., Reier, T., and Strasser, P. (2016). Tuning the catalytic activity and selectivity of Cu for CO<sub>2</sub> electroreduction in the presence of halides. *ACS Catal.* **6**, 2136–2144.
33. Tao, Z., Wu, Z., Wu, Y., and Wang, H. (2020). Activating copper for electrocatalytic CO<sub>2</sub> reduction to formate via molecular interactions. *ACS Catal.* **10**, 9271–9275.
34. Tan, Y.C., Lee, K.B., Song, H., and Oh, J. (2020). Modulating local CO<sub>2</sub> concentration as a general strategy for enhancing C–C coupling in CO<sub>2</sub> electroreduction. *Joule* **4**, 1104–1120.
35. Gong, Y.-N., Jiao, L., Qian, Y., Pan, C.-Y., Zheng, L., Cai, X., Liu, B., Yu, S.-H., and Jiang, H.-L. (2020). Regulating the coordination environment of MOF-templated single-atom nickel electrocatalysts for boosting CO<sub>2</sub> reduction. *Angew. Chem. Int. Ed. Engl.* **59**, 2705–2709.
36. Zhang, Y., Jiao, L., Yang, W., Xie, C., and Jiang, H.-L. (2021). Rational fabrication of low-coordinate single-atom Ni electrocatalysts by MOFs for highly selective CO<sub>2</sub> reduction. *Angew. Chem. Int. Ed. Engl.* **60**, 7607–7611.
37. Jiao, L., Wang, J., and Jiang, H.-L. (2021). Microenvironment modulation in metal–organic framework-based catalysis. *Acc. Mater. Res.* **2**, 327–339.
38. Gu, Z., Shen, H., Shang, L., Lv, X., Qian, L., and Zheng, G. (2018). Nanostructured copper-based electrocatalysts for CO<sub>2</sub> reduction. *Small Methods* **2**, 1800121.
39. Shen, H., Li, Y., and Sun, Q. (2017). CO<sub>2</sub> electroreduction performance of phthalocyanine sheet with Mn dimer: a theoretical study. *J. Phy. Chem. C* **121**, 3963–3969.
40. Yang, X.-L., Xie, M.-H., Zou, C., He, Y., Chen, B., O’Keeffe, M., and Wu, C.-D. (2012). Porous metalloporphyrinic frameworks constructed from metal 5,10,15,20-tetrakis(3,5-bis(carboxyphenyl))porphyrin for highly efficient and selective catalytic oxidation of alkylbenzenes. *J. Am. Chem. Soc.* **134**, 10638–10645.
41. Sun, L., Reddu, V., Fisher, A.C., and Wang, X. (2020). Electrocatalytic reduction of carbon dioxide: opportunities with heterogeneous molecular catalysts. *Energy Environ. Sci.* **13**, 374–403.
42. Diercks, C.S., Liu, Y., Cordova, K.E., and Yaghi, O.M. (2018). The role of reticular chemistry in the design of CO<sub>2</sub> reduction catalysts. *Nat. Mater.* **17**, 301–307.
43. Kornienko, N., Zhao, Y., Kley, C.S., Zhu, C., Kim, D., Lin, S., Chang, C.J., Yaghi, O.M., and Yang, P. (2015). Metal–organic frameworks for electrocatalytic reduction of carbon dioxide. *J. Am. Chem. Soc.* **137**, 14129–14135.
44. Huang, Q., Li, Q., Liu, J., Wang, Y.R., Wang, R., Dong, L.Z., Xia, Y.H., Wang, J.L., and Lan, Y.-Q. (2019). Disclosing CO<sub>2</sub> activation mechanism by hydroxyl-induced crystalline structure transformation in electrocatalytic process. *Matter* **1**, 1656–1668.
45. Meng, Z., Luo, J., Li, W., and Mirica, K.A. (2020). Hierarchical tuning of the performance of electrochemical carbon dioxide reduction using conductive two-dimensional metallophthalocyanine based metal–organic frameworks. *J. Am. Chem. Soc.* **142**, 21656–21669.
46. Karas, L.J., Wu, C.-H., Das, R., and Wu, J.I.C. (2020). Hydrogen bond design principles. *Wiley Interdiscip. Rev. Comput. Mol. Sci.* **10**, e1477.
47. Zhao, Y., Wang, J., and Pei, R. (2020). Micron-sized ultrathin metal–organic framework sheet. *J. Am. Chem. Soc.* **142**, 10331–10336.
48. Zhao, Y., Fan, G., Yang, L., Lin, Y., and Li, F. (2018). Assembling Ni–Co phosphides/carbon hollow nanocages and nanosheets with carbon nanotubes into a hierarchical necklace-like nanohybrid for electrocatalytic oxygen evolution reaction. *Nanoscale* **10**, 13555–13564.
49. Liu, P., and Hensen, E.J.M. (2013). Highly efficient and robust Au/MgCuCr<sub>2</sub>O<sub>4</sub> catalyst for gas-phase oxidation of ethanol to acetaldehyde. *J. Am. Chem. Soc.* **135**, 14032–14035.
50. Lee, S.Y., Jung, H., Kim, N.-K., Oh, H.-S., Min, B.K., and Hwang, Y.J. (2018). Mixed copper states in anodized Cu electrocatalyst for stable and selective ethylene production from CO<sub>2</sub> reduction. *J. Am. Chem. Soc.* **140**, 8681–8689.
51. Yi, J.-D., Xie, R., Xie, Z.-L., Chai, G.-L., Liu, T.-F., Chen, R.-P., Huang, Y.-B., and Cao, R. (2020). Highly selective CO<sub>2</sub> electroreduction to CH<sub>4</sub> by in situ generated Cu<sub>2</sub>O single-type sites on a conductive MOF: stabilizing key intermediates with hydrogen bonding. *Angew. Chem. Int. Ed. Engl.* **59**, 23641–23648.
52. Song, Y., Chen, W., Zhao, C., Li, S., Wei, W., and Sun, Y. (2017). Metal-free nitrogen-doped mesoporous carbon for electroreduction of CO<sub>2</sub> to ethanol. *Angew. Chem. Int. Ed. Engl.* **56**, 10840–10844.
53. Ye, L., Ying, Y., Sun, D., Zhang, Z., Fei, L., Wen, Z., Qiao, J., and Huang, H. (2020). Highly efficient porous carbon electrocatalyst with controllable N-species content for selective CO<sub>2</sub> reduction. *Angew. Chem. Int. Ed. Engl.* **59**, 3244–3251.